

Development of a Couette–Taylor flow device with active minimization of secondary circulation

E. Schartman,¹ H. Ji,² and M. J. Burin³

¹Princeton University, MS30 P.O. Box 451, Princeton, New Jersey 08543-0451, USA

²Princeton Plasma Physics Laboratory, MS17 P.O. Box 451, Princeton, New Jersey 08543-0451, USA

³Department of Physics, California State University, Science Hall 2, #215, San Marcos, 333 S. Twin Oaks Valley Rd., San Marcos, California 92096-0001, USA

(Received 17 July 2008; accepted 13 January 2009; published online 13 February 2009)

A novel Taylor–Couette experiment has been developed to produce rotating shear flows for the study of hydrodynamic and magnetohydrodynamic instabilities which are believed to drive angular momentum transport in astrophysical accretion disks. High speed, concentric, corotating cylinders generate the flow where the height of the cylinders is twice the radial gap width. Ekman pumping is controlled and minimized by splitting the vertical boundaries into pairs of nested, differentially rotating rings. The end rings and cylinders comprise four independently driven rotating components which provide flexibility in developing flow profiles. The working fluids of the experiment are water, a water-glycerol mix, or a liquid gallium alloy. The mechanical complexity of the apparatus and large dynamic pressures generated by high speed operation with the gallium alloy presented unique challenges. The mechanical implementation of the experiment and some representative results obtained with laser Doppler velocimetry in water are discussed. © 2009 American Institute of Physics. [DOI: 10.1063/1.3077942]

I. INTRODUCTION

The investigation of fluid instabilities which may be responsible for the turbulent transport of angular momentum in accretion disks^{1,2} requires establishing quiescent shear flow at high Reynolds number. The instabilities which the Princeton magnetorotational instability (MRI) experiment is designed to study are subcritical hydrodynamic instability^{3,4} (SHI) and MRI.⁵ In SHI, it is proposed that finite amplitude disturbances cause the fluid to transition nonlinearly to a turbulent state. Transitions of this nature are responsible for the turbulence seen in plane Couette and Poiseuille flow.⁶

Accretion disks are combinations of plasma, neutral gas, and dust in orbit about, and slowing falling on to, massive compact central objects. The angular velocity in the disk follows $\Omega \sim r^{-3/2}$, while angular momentum is $l \sim r^{1/2}$. The rate of infall is governed by the transport of angular momentum out of the disk. The source of the transport cannot be laminar viscosity because timescales for processes such as star formation are orders of magnitude too large to explain observations. Centrifugal hydrodynamic instability is ruled out by the positive radial gradient of angular momentum.¹ The MRI is a linear instability in which a weak magnetic field uses the negative angular velocity gradient as a source of free energy to transport angular momentum.⁵ MRI is now believed to be the primary transport mechanism in accretion disks, but SHI remains of interest for some protostellar disks which may be too poorly ionized to be unstable to the MRI.³

It is believed that MRI and SHI can be produced in laboratory shear flows. The Princeton MRI experiment was developed to produce the shear flows required for these instabilities while minimizing secondary flows which might mask their presence or suppress them. For SHI studies the

working fluids are water and a water-glycerol mixture with kinematic viscosity $\nu_{\text{mix}} \approx 15\nu_{\text{water}}$. MRI experiments require a magnetic field and a conducting fluid. The magnets and associated diagnostics for the magnetohydrodynamic experiments are not discussed here. Our conducting fluid is a eutectic GaInSn alloy⁷ with kinematic viscosity $\nu_{\text{Ga}} \approx 0.3\nu_{\text{water}}$ and density $\rho = 6.3 \times 10^3 \text{ kg/m}^3$ at a temperature of 25 °C.

Flows developed between concentric spinning cylinders were originally investigated by Couette⁸ and Mallock⁹ for measuring viscosity. Theoretically, for cylinders of infinite axial extent, the flow profile is determined by the purely viscous radial transport of angular momentum, which yields the ideal circular Couette solution for the angular velocity, Ω ,

$$\Omega(r) = a + b/r^2. \quad (1)$$

The constants a and b are determined by the cylinder speeds, Ω_1 and Ω_2 .

In the absence of viscosity, if the angular momentum is a decreasing function of radius, $\partial(r^2\Omega)^2/\partial r < 0$, the flow is linearly unstable.¹⁰ The onset of instability is delayed by viscosity.¹¹ Unstable flow proceeds to fully developed turbulence through a sequence of bifurcations, and is the subject of a great deal of theory and experiment.¹² The majority of experiments are performed with the outer cylinder held fixed and the inner cylinder speed slowly increased through the sequence of instabilities. A few experiments have also been performed with the inner cylinder at rest and the outer cylinder rotating. Although the flow in this case is linearly stable, a transition to turbulence has been observed.^{13,14} This transition has been attributed to SHI,^{3,4,15} but also to a Kelvin–Helmholtz type of instability.¹⁶ Fewer

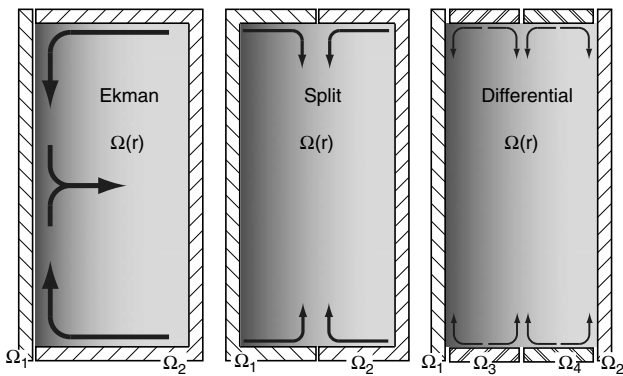


FIG. 1. Illustration of the influence of the end cap boundary conditions on flow developed between the cylinders. Arrows indicate flows attached to the boundaries in the r - z plane, and also approximate locations of detachment. Left: when the end caps corotate with the outer cylinder, the total velocity difference between the end caps and the bulk flow is greatest, producing a maximum advective torque on the flow. In a small aspect ratio device a large-scale two cell meridional circulation results from the Ekman flows generated by each end cap meeting at the midplane of the inner cylinder. Right: simulations showed that the net torque induced by Ekman pumping at the end caps would be substantially reduced by dividing the caps into differentially rotating rings. The two cell circulation is then replaced by multiple smaller cells. The two ring configuration was chosen as a compromise between mechanical complexity and improved approximation to ideal Couette flow. As shown, the center radius of each ring is rotating at the speed of the bulk fluid above it, and the boundary layer flows away from those points. Middle: many Taylor–Couette experiments fix one half of the end cap to each cylinder (Ref. 15). The simulations¹⁸ showed that this would not be an effective strategy for our small aspect ratio device.

experiments^{15,17,18} have been performed in the regime in the linearly stable regime with $0 < \Omega_2 < \Omega_1$, which is most analogous to accretion disk flows. Our experiments¹⁹ in this regime find no evidence of a subcritical transition up to Reynolds number $\text{Re} = (\Omega_1 - \Omega_2)(r_2 - r_1)(r_2 + r_1)/2\nu \sim 10^6$.

A discussion of the relation of this experiment’s unique geometry to the broad array of experiments performed on the Taylor–Couette flow can be found in Ref. 20. Little investigation has been done for linearly stable flow profiles with both cylinders rotating.^{15,17,18}

When the cylinders are of finite height the flow profile is distorted from the ideal Couette solution by the influence of the cylinder end caps. The primary source of this distortion is Ekman pumping²¹ by the viscous boundary layer which corotates with the end caps. In the bulk of the fluid, pressure balances the centrifugal force generated by the azimuthal velocity of circular Couette flow $v_\theta = r\Omega(r)$, where $\Omega(r)$ is given by Eq. (1). The no-slip condition at the end cap boundary is $v_\theta = r\Omega_{\text{cap}}$. The pressure is approximately uniform vertically so the difference in centrifugal force generates a radial secondary flow, see Fig. 1. In the case in which the end cap rotates slower than the bulk fluid, the radial flow is directed inward. Incompressibility of the fluid requires that the radial flow transition to an axial one at the inner cylinder. In a short apparatus the axial flows from the boundaries may meet at the cylinder midplane, thereby establishing a large meridional circulation in the r - z plane. The presence of this circulation violates the assumption under which Eq. (1) was derived.

To minimize the effect of the boundaries most Taylor–Couette experiments use a large aspect ratio, $h/(r_2 - r_1)$,

where h is the axial extent of the cylinders. Taylor¹¹ used aspect ratios larger than 100 in order to minimize the dynamical role of the end caps. We chose to use a small aspect ratio device in order to minimize the volume, and therefore expense, of GaInSn alloy. A prototype experiment was constructed to measure the impact of the Ekman circulation on the flow profile.¹⁸ We found that the mean radial profile of v_θ differed significantly from the ideal solution, Eq. (1). In particular, the monotonically decreasing nature of the profile was replaced by an unstable region near the inner cylinder and a solid-body-like rotation near the outer cylinder. A two-dimensional simulation demonstrated that the meridional flows due to Ekman pumping at the end caps joined at the inner cylinder midplane to produce a radial jet, illustrated in the left panel of Fig. 1.

The importance of reducing Ekman pumping in the experimental search for the MRI is threefold. First, Ekman pumping may reduce the flow shear as measured in the prototype. It is critical to maximize the flow shear because the MRI growth rate is proportional to the gradient of the angular velocity.² If the MRI growth rate falls below the resistive decay rate of the liquid metal, the instability will not be established. Second, in the presence of Ekman pumping the sign of the angular velocity gradient may become positive as in the solid-body-like region of the prototype. A positive gradient is stable to the MRI. Third, the Ekman circulation may directly interact with the magnetic field, in which case it might be very difficult to separate the effects of the secondary flow from that those of the MRI.

The simulations¹⁸ showed that the approximation to the ideal Couette flow could be significantly improved by dividing the end caps into multiple independent rings. The torque exerted on the fluid by the boundary layer is proportional to the magnitude of the velocity difference between the end cap and the bulk flow.¹⁸ The design of the current apparatus is derived from those multiple-ring simulations. The right panel of Fig. 1 illustrates the idea. Differentially rotating rings enable us to minimize the average velocity difference between the end cap and the bulk flow, thereby reducing the net torque. The simulations showed that two independent rings were sufficient to produce a satisfactory approximation to the ideal Couette profile. Burin *et al.*²⁰ presented initial results from the current apparatus demonstrating the effectiveness of the two end rings.

II. THE PRINCETON MRI EXPERIMENT

A. Apparatus

The Princeton MRI experiment consists of a rotating apparatus which is mounted vertically in a rigid frame. The base of the frame is bolted to the laboratory floor, but can be rotated 90° for maintenance. The frame also provides mounting support for drive motors and magnet coils. The rotating apparatus includes the inner and outer cylinders and the four end rings (two nested pairs located at the top and bottom of the cylinders). The constraints which drove the design of the rotating apparatus were as follows: (1) The experiment must be capable of achieving a Reynolds number of $\text{Re}_{\text{max}} \approx 10^7$ in operation with the GaInSn alloy. (2) The outer cylinder must

TABLE I. Radii and maximum rotation rate of experiment components. For the inner and outer rings the radius is the midradius of the ring.

Component	Radius (mm)	$\Omega_{\max}/2\pi$ (s ⁻¹)
Inner cylinder	70.6	66.7
Inner ring	101.5	24.3
Outer ring	167.8	6.7
Outer cylinder	203.0	9.0
Cylinder height	280.0 mm	

withstand the dynamic pressure generated by the azimuthal velocity profile of GaInSn. (3) The apparatus materials must be chemically compatible with GaInSn. (4) The rotating components must be sealed to prevent GaInSn from being lost and also to minimize oxygen leaks into the experiment to minimize oxidation of the alloy.

The radii and height of the cylinders was chosen to maximize the radial magnetic diffusion time relative to the growth time of the MRI.² The experiment geometry and maximum speeds are listed in Table I. The dynamic pressure for a stable flow is $P(r) = \rho \int_{r_1}^r v_{\theta}^2(r) / r dr$, where ρ is the fluid

density. For GaInSn at maximum speed the pressure at the outer cylinder wall is $P_{\max} \approx 2.5$ MPa.

Rotating components of the experiment, and bearing support structure are diagrammed in Fig. 2. To withstand P_{\max} , a pressure vessel is formed of the outer cylinder and caps which are drawn against the cylinder by 16 12.7 mm diameter stainless steel tie rods. For the SHI experiments using water the outer cylinder is an acrylic annulus, 25 mm thick. To avoid possible crazing failure of the acrylic under full speed GaInSn operation, the acrylic annulus is replaced by a stainless steel one of 5 mm thickness. The top and bottom caps of the vessel are 102 mm thick acrylic disks. Within this pressure vessel are submerged the remaining rotating components, namely the inner cylinder and four end rings. These submerged components are suspended from nested concentric stainless steel axles which pass through the top cap of the pressure vessel. Spring energized lip seals are used to seal the axles where they pass out of one another. The outer cylinder is supported vertically by a 35 mm diameter stainless steel axle which threads the entire length of the experiment.

Each suspended component is supported by two bear-

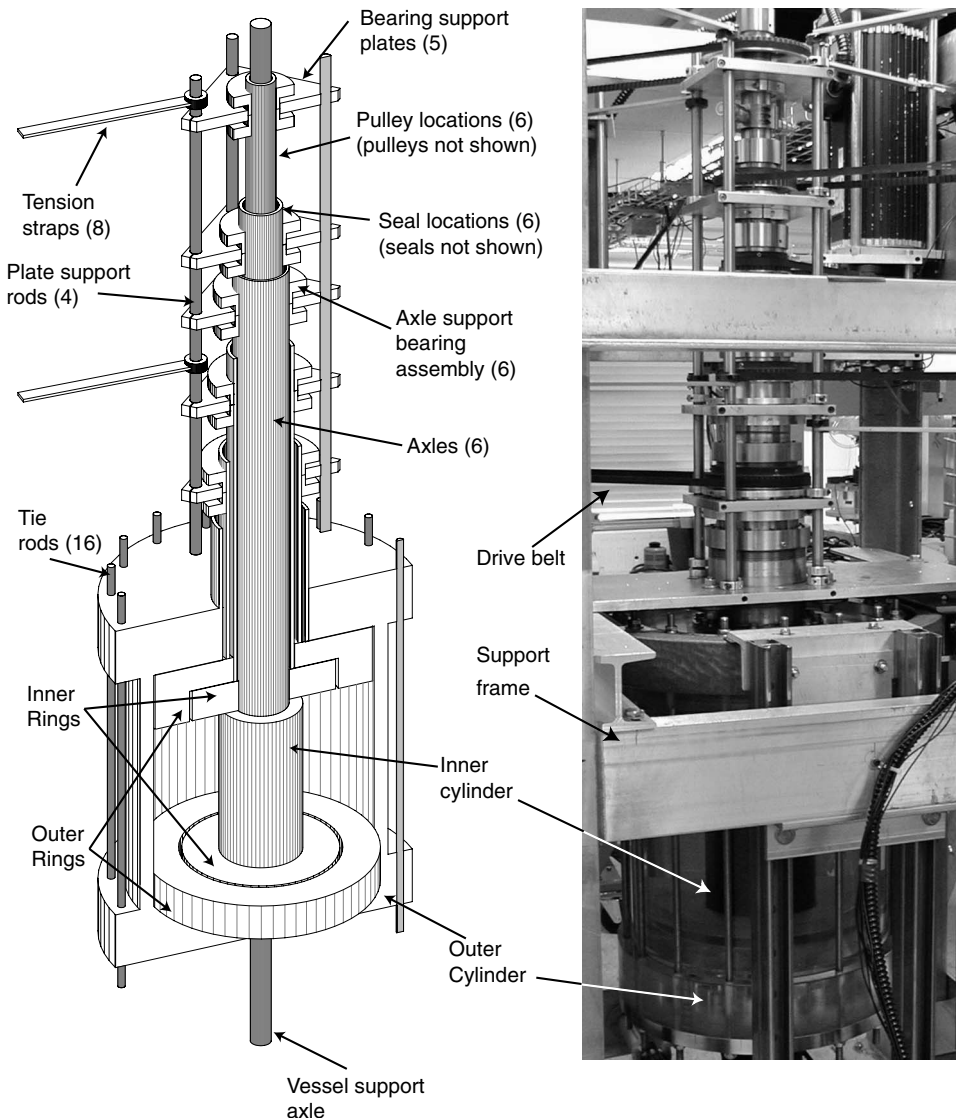


FIG. 2. Select components of the Princeton MRI experiment.

ings. Within the submerged end of the component there is a plain bearing made of Techtron HPV [poly(tetrafluoroethylene) (PTFE)-filled polyphenylsulfide] which only provides support for radial loads. The Techtron HPV was chosen for its combination of wear resistance, high $(PV)_{\max}$ (the maximum combination of bearing load and speed which can be maintained for a nominal bearing lifetime) rating, availability in large extrusions, and compatibility with nonaqueous environments. The mating surface of each bearing is the outer diameter of the next smaller axle. The radial clearance between the bearing and its mating axle is large by the standards of precision high speed machinery—in some cases the clearance is as large as 0.15 mm, which is required to allow the mating axle to pass its entire length through the bearing during assembly. The sum of these bearing clearances contributes to a visible runout of the inner cylinder of approximately 0.8 mm. Contrary to expectation, this runout contributes positively to the experiment performance by actively disrupting the Ekman circulation.

The nonsubmerged end of each axle is clamped to the inner diameter of a low-profile angular contact ball bearing. This bearing serves three functions: support of the component against all thrust loads, support against radial loads (such as drive belt tension), and precise radial location of the axle for proper operation of the rotating seals. The outer diameter of each ball bearing is captured by an aluminum plate which is clamped at each corner to a precision ground steel rod. The tolerance of the location of the bearing bore relative to the rods is 0.013 mm. The combination of bearing plates and rods comprises the “bearing stack” which has a height of 900 mm. When the clamp bolts which fix the plate to the rods are loose, the vertical location of the plate can be adjusted to precisely set the vertical clearances between the various end rings and cylinders. This is a critical step in the assembly process because the combination of dynamic loads and residual axial play may allow binding between the components to occur. Finally, the large length of the bearing stack allows plate-to-plate deflection which may exceed the tolerances of the rotating seals. To minimize overall deflection from the stack, eight tensioning straps attach the mid- and upper points of the stack to the experiment frame. Adjustment of the strap tensions pulls the stack into proper alignment.

1. Seals

The rotating seals between axles are provided by Variseal spring energized lip seals, manufactured by Trelleborg Sealing Solutions. The seal lip is Turcon T07, a proprietary carbon-filled PTFE compound with high wear resistance, dynamic pressure rating of 15 MPa, and low friction. A helical spring occupies an elliptical cavity between the seal lip and seal body. The spring actively pushes the lip against the sealed surface which improves sealing at low pressure and increases tolerance to runout and ellipticity of the sealed shaft. The axles were coated with 0.03 mm thick chrome plate to increase wear resistance where the seal lips make contact. The $(PV)_{\max}$ rating of the seals with good lubrication is 5 MPa m/s. Unlike most rotary seal applications, in our experiment the seal body rotates as well as the sealed sur-

TABLE II. Seal parameters. “Joint” labels the two axles which are being sealed, OC (IC) refers to the outer (inner) cylinder, and OR (IR) are the outer (inner) rings. V_{\max} is the maximum surface speed for a seal with lip diameter r_s . TIR is the total indicated runout specification of the seal. A proper seal cannot be maintained if the combination of radial offset of the two axles and the ellipticity of the sealed axle exceed the TIR.

Joint	r_s (mm)	V_{\max} (m/s)	TIR (mm)
OC-OR	70	0.9	0.20
OR-IR	57	6.3	0.18
IR-IC	48	12.7	0.15
IC-IR	48	12.7	0.15
OR-IR	48	5.3	0.15
OR-OC	17	0.2	0.05

face. This significantly reduces the surface speed experienced by the seal lip. The seal’s tolerance to shaft runout and maximum surface speed is summarized in Table II. The velocity difference between the inner cylinder axle and inner ring axles exceeds the seals’ 2 m/s maximum surface speed for rotary motion. This reduces the service life of these seals to less than 100 h of operation.

Five of the six seals are held concentric (to within their total indicated runout tolerance) using delrin or stainless steel adapters and also through minimization of bearing stack deflection. The small diameter of the sixth seal requires a factor of 3 smaller runout than the other components. To satisfy this requirement the seal holder incorporates a ball bearing. The inner race of the ball bearing forces the 2 m long center axle to run concentric to the seal.

The seals are cooled and lubricated with automatic transmission fluid which is blown on the axles using compressed air jets. The compressed air is required to overcome windage from the rotating shafts which would otherwise greatly reduce the quantity of coolant reaching the seals. The coolant also lubricates the ball bearings of the bearing stack. Coolant which is shed from the rotating axles is captured by a screen which channels it to a sump, from which it is recirculated by a pump. The coolant rate to each seal is controlled by a needle valve.

2. Drives and control

The inner cylinder is driven by a 7.5 kW ac motor, while the other three components are driven with dc motors ranging in power from 0.6 to 2.3 kW. Timing belts and pulleys transmit power from the motors to the component axles. The upper and lower inner rings are driven by a single motor, as are the two outer rings. A National Instruments NI-7344 four-axis motion control card is used to control the rotation of the experiment. Optical encoders mounted on each motor provide feedback for the motion control card. The card generates analog control voltages for the four motor amplifiers. The card computes a following error for each axis which is the difference between the current and target velocities. If the following error exceeds a maximum value the servo loop is shut down. This shutdown mechanism prevents damage to the experiment in such cases as binding between components, or overheating of seals due to coolant loss.

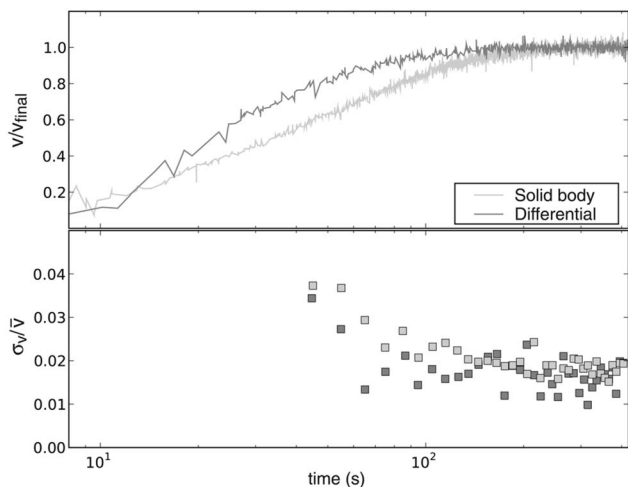


FIG. 3. Comparison of fluid spin-up to solid body (light) and differential rotation (dark) at $r=180$ mm. The fluid is nearly at rest prior to start of rotation at time $t=0$. For $t>0$, for the solid body case the components are accelerated to $\Omega_1=\Omega_3=\Omega_4=\Omega_2=0.88$ s $^{-1}$. In the differential case, the components are accelerated to $\Omega_1=6.67$, $\Omega_3=2.43$, $\Omega_4=0.67$, $\Omega_2=0.88$ s $^{-1}$. Upper panel: velocity, normalized by the final speed of the fluid, $v_{\text{final}}=v_{\theta}(t\rightarrow\infty)$. Lower panel: fluctuation levels, $\sigma_v/\bar{v}_{\theta}$. We wait 300 s before starting measurements of the flow. The velocity is measured using LDV, see Sec. III. The minimum fluctuation level of approximately 0.02 is limited by the optical properties of the acrylic outer cylinder.

All profiles are reached by an impulsive change in boundary rotation speeds. The experiment was most often started from rest, but transitions from solid body to differential rotation were also common. The time scale of flow spin-up is determined by Ekman pumping, although instabilities at the walls may also contribute to the early spin-up. The Ekman timescale is $\tau_E \sim (L^2/\nu\Omega_2)^{1/2}$,²¹ where L is a characteristic length scale. An Ekman layer forms at the upper and lower cylinder caps, so we choose L to be the half height of the cylinders: $L=132$ mm. For spin-up to solid body rotation at $\Omega_2=53$ rpm, $\tau_E \approx 60$ s. We wait approximately five Ekman times for the flow to equilibrate before starting velocity measurements, see Fig. 3.

III. LASER DOPPLER VELOCIMETRY

Laser Doppler velocimetry (LDV)²² uses coherent scattering of laser light from tracer particles entrained in a flow to obtain a measurement of the fluid velocity. Our experiments used a Dantec dynamics flow-lite two component LDV. The measured velocities in this experiment are v_{θ} when the diagnostic views the fluid radially through the outer cylinder wall, and v_{θ} and v_r when the fluid is viewed axially through the end rings and outer cylinder bottom cap. In the radial orientation v_z was also measured. However, the measurement volume of v_z did not coincide with that of v_{θ} , and was often outside of the cylinder gap. We do not present the v_z data.

The particles used for our experiment were silver-coated hollow glass spheres with a density of 1.6 mg/mm 3 and a mean diameter of 15 μm . The total volume of the water used in the experiment is greater than 3×10^7 mm 3 while the volume of particles added did not exceed 20 mm 3 . Any ve-

locity error due to particle slip relative to the fluid is negligible, as is any effect on the mean flow due to the presence of the particles.^{23,24}

A. Calibration

In this experiment, the primary sources of error in the LDV measurement are due to optical properties of the acrylic outer cylinder. The errors arise from the mean curvature of the cylinder when the fluid is measured radially, misalignment of the probe head and defects in the optical path which arise from deviations of the wall due to the manufacturing process and stress induced variations in the index of refraction of the acrylic. Mean deviation due to these effects can be removed through calibration. However, the optical defects also broaden the sample distribution of the velocity measurement, which cannot be eliminated. They also introduce a systematic offset in correlation between the radial and azimuthal velocities.

Calibration of LDV data were done using solid body rotation in which the rotation rates of the cylinders and rings are equal: $\Omega_1=\Omega_3=\Omega_4=\Omega_2$, Ω_3 and Ω_4 are the speeds of the inner and outer ring, respectively. In solid body rotation, $v_{\theta}(r)=r\Omega$. During these experiments, uncertainty in the magnitude of Ω is less than 1% while it varies by less than 0.1%. To ensure that the water was fully equilibrated with the boundaries, a minimum of 2 min were allowed to pass between the start of component rotation and the start of LDV operation. The measured velocities were then compared to the expected values based on the known rotation rate.

When the LDV diagnostic is oriented axially to measure v_{θ} and v_r , the beam path passes through the cylinder bottom cap and outer ring. Attenuation of the laser intensity due to the four boundary crossings limits the data rate to ≈ 1 Hz. For the previously reported¹⁹ measurement of the radial-azimuthal component of Reynolds stress, we required of order 10^3 velocity samples per fluid profile. Because of this time demand, LDV was performed at only one radial location in this orientation. The LDV probe head was oriented such that the beam bisector was approximately normal to the acrylic surfaces. Comparison with the expected velocity value for solid body rotation revealed an offset of about 3% in the magnitude of the v_{θ} .

When the LDV was setup to measure radial profiles of v_{θ} , the beam probe head is oriented to view the fluid through the curved outer cylinder wall. The laser paths for the velocity component tangent to the azimuthal angle enter and exit the cylinder wall at non-normal incidence. As the probe is scanned radially the angles of incidence change which alters both the radial location and magnitude of the velocity measurement. In principle, these angles can be calculated as a function of the distance from the probe head to the outer surface of the cylinder and a correction applied to the radius and velocity. Because of the difficulty of ensuring normal orientation of the probe head with respect to the cylinder surface, and because the radius of curvature of the cylinder is much greater than the beam separation, we used linear approximations to apply corrections to position and velocity.

The probe head is mounted on a three-axis traversing stage. The y -axis of the stage is aligned with r , the locations

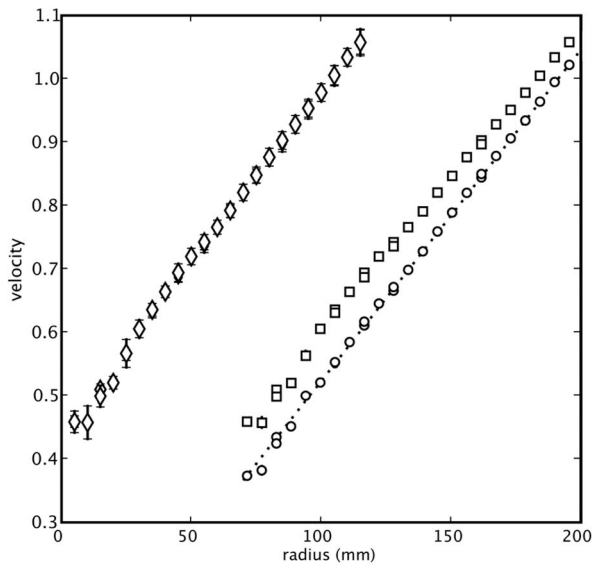


FIG. 4. Calibration steps for radially acquired velocity data. Raw data (\diamond) requires calibration of both radius and velocity. The radial calibration is first applied (\square) then the velocity calibration is applied (\circ). The dashed line is solid body rotation. For clarity, fluctuation levels are shown only on the raw data.

of the inner and outer cylinder at y_1 and y_2 , respectively. The stage x -axis is aligned to measure azimuthal velocity, v_θ . The solid body rotation speed is Ω . The linear corrections are as follows:

$$r = r_2 - (y_2 - y) \left(\frac{r_2 - r_1}{y_2 - y_1} \right), \quad (2)$$

$$v_\theta = v_x \left(\frac{r\Omega}{c_0 + c_1 r} \right), \quad (3)$$

the constants c_0 and c_1 are determined by a least-squares fit to the velocities after the radial correction has been applied. The steps of the calibration process are diagrammed in Fig. 4. Residual error after calibration is $<1\%$ over the radius range $100 \text{ mm} \leq r \leq 203 \text{ mm}$ and $<5\%$ in the range $70.6 \text{ mm} < r < 100 \text{ mm}$. The larger error near the inner cylinder is due to lower data rates and larger measurement scatter.

IV. PERFORMANCE

In this section we present examples of the effect of the end rings on the mean azimuthal flow profile, and scaling of the profile with Re . To illustrate control of boundary layer circulation, the radial profile of v_θ for the three end ring configurations of Fig. 1 are studied. The first configuration is with the end rings corotating with the outer cylinder and is expected to be dominated by meridional circulation cells driven by Ekman pumping. For convenience we refer to this as the “Ekman” configuration. This mode of operation is expected to reproduce the results of the prototype experiment.¹⁸ In the second, which we refer to as a “split” configuration, the inner (outer) ring corotates with the inner (outer) cylinder. This configuration matches many Taylor–Couette experiments at larger aspect ratios, e.g., Richard.¹⁵

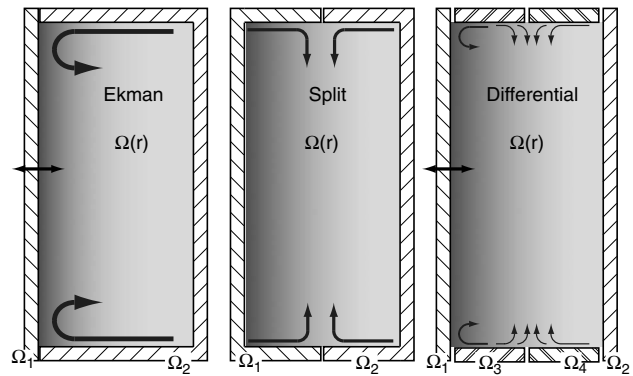


FIG. 5. Fig. 1 modified to reflect our knowledge of the impact of the end rings on the bulk flow. Left panel: when the end rings corotate with the outer cylinder, differential rotation of the inner cylinder with respect to the inner ring disrupts the Ekman layer. The large-scale two cell circulation is not established. The result is a significant improvement in the approximation of the ideal Couette flow over other small aspect ratio experiments (Ref. 18). The disruption is due to the runout of the inner cylinder, where the runout is symbolized by the double-headed arrow. Right panel: differential rotation of the end rings optimized to produce the best approximation to the ideal Couette flow. As in the left panel, the boundary layer is shed by the runout. In addition, the outer ring is rotating slower than the outer cylinder. Therefore, there is no radius at which the outer ring rotates at the same speed as the bulk flow. This prevents the boundary layer from penetrating into the bulk flow as occurs for the inner ring, see Fig. 7. There is some evidence that the Ekman layer detaches from the end rings near the ring gap in a region which is about 20 mm in radial extent (Ref. 25). This idea is shown schematically with the multiple small arrows above the outer ring.

The final configuration features the end rings rotating independent of the cylinders (and each other) to produce the best possible approximation to the ideal flow profile, Eq. (1).

The illustration of Fig. 1 is reproduced in Fig. 5 after incorporating our knowledge of how the end rings impact the flow. Radial profiles of v_θ for the three configurations are plotted in Fig. 6. The most striking feature of the apparatus operation is that the Ekman configuration is a far better approximation to the ideal Couette profile than the Split case. This contradicts our expectation based on the prototype experiment, and also the results of many Taylor–Couette experiments. Richard¹⁵ compared the Ekman and Split styles in his experiment and found that the split style best approximated the ideal flow. We believe this difference in operation is due to the runout of the inner cylinder. In the left panel of Fig. 5, we indicate the runout by the double-headed horizontal arrow. For Ekman pumping to establish a large-scale meridional circulation, the boundary layer at the end caps must transition to the inner cylinder. The runout disrupts the transition, leaving the boundary layer confined near the end caps. When we run in the Split style, there is no differential rotation of the cylinder and therefore no disruption of circulation. We also note that in the split case the angular momentum contributed to the bulk flow by the inner ring has caused the flow to become unstable. This is signaled by the centrifugally unstable shear layer which must be present to connect the bulk flow to the outer cylinder at $r > 200 \text{ mm}$.

Finally, we optimized the end ring speed to produce the best approximation to the ideal Couette flow. This profile is indicated by the triangles in Fig. 6, and the action of the end rings is sketched in the right most panel of Fig. 5. In addition to the boundary flow disruption by the inner cylinder, we

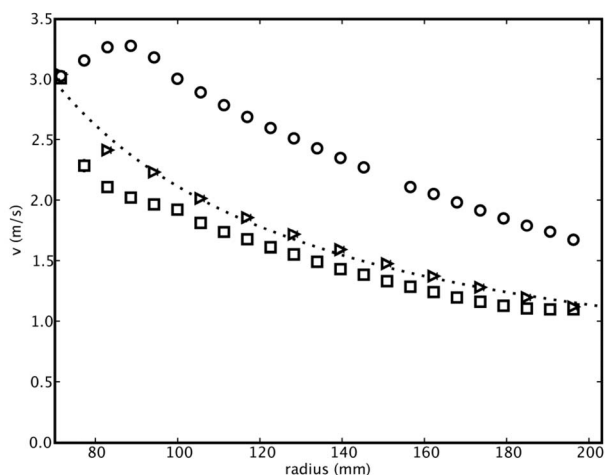


FIG. 6. Comparison of operation of the experiment at $Re=6.6 \times 10^5$, demonstrating the effect of end ring speeds on the mean profile. The effect of Ekman pumping is demonstrated when the end rings corotate with the outer cylinder (\square). The components speeds are as follows: $[\Omega_1, \Omega_3, \Omega_4, \Omega_2] = 6.67, 0.88, 0.88, 0.88 \text{ s}^{-1}$. Operation with the inner (outer) ring corotating with the inner (outer) cylinder is labeled with (\circ). The components speeds are as follows: $[\Omega_1, \Omega_3, \Omega_4, \Omega_2] = 6.67, 6.67, 0.88, 0.88 \text{ s}^{-1}$. When the end rings rotate at intermediate speeds (\triangleright) an excellent approximation to the ideal profile is achieved. The component speeds are as follows: $[\Omega_1, \Omega_3, \Omega_4, \Omega_2] = 6.67, 2.43, 0.67, 0.88 \text{ s}^{-1}$. The dashed line is the ideal profile, no fit has been performed. Random uncertainty in the mean is smaller than the symbol size.

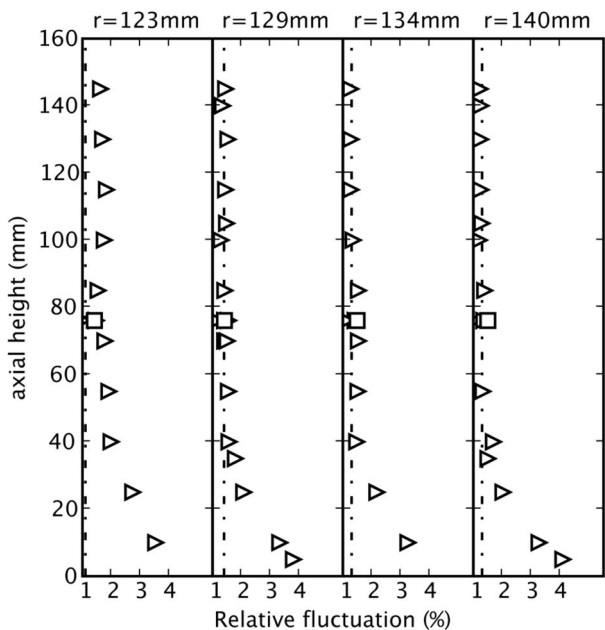


FIG. 7. Vertical scans through the optimized profile of Fig. 6 of relative fluctuation amplitude: $\sigma_{v_\theta}/\bar{v}_\theta$. Four radial locations near the gap between the inner and outer end rings are shown: $r=123, 129, 134, 140 \text{ mm}$. The axial height is measured relative to the upper surface of the lower end rings. Solid body fluctuation levels are indicated by the vertical dashed lines. A single height for the Ekman profile is also plotted (\square). At $r=123 \text{ mm}$, the boundary speed $r\Omega_3$ is approximately equal to that of the bulk profile $r\Omega(r)$, which allows fluctuations from the boundary to penetrate vertically through the whole flow.

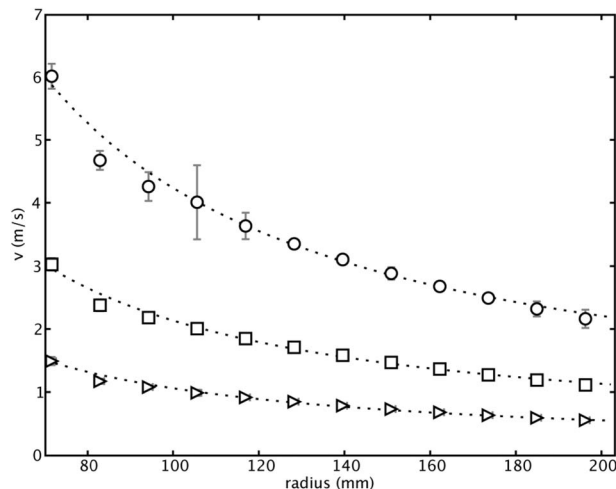


FIG. 8. Scaling with Re of the optimized profile shown in Fig. 6. (\triangleright) $Re = 3.3 \times 10^5$, with speeds $[\Omega_1, \Omega_3, \Omega_4, \Omega_2] = 3.33, 1.22, 0.33, 0.44 \text{ s}^{-1}$. (\square) $Re = 6.6 \times 10^5$, with speeds $[\Omega_1, \Omega_3, \Omega_4, \Omega_2] = 6.67, 2.43, 0.67, 0.88 \text{ s}^{-1}$. (\circ) $Re = 1.3 \times 10^6$, with speeds $[\Omega_1, \Omega_3, \Omega_4, \Omega_2] = 13.33, 4.86, 1.34, 1.76 \text{ s}^{-1}$. Scaling the component rotation speeds by a constant factor reproduces the agreement with the ideal profiles (dashed lines). Error bars represent random uncertainty in the mean.

found through trial and error that choosing $\Omega_4 < \Omega_2$ produced the best results. In this case the outer ring has no radius at which its speed matches that of the bulk flow. This prevents boundary layers from significantly penetrating in to the bulk flow, and they instead remain confined to within $\approx 40 \text{ mm}$ of the rings, see Fig. 7.

Figure 6 data was acquired with the LDV oriented radially and calibrated as discussed in Sec. III. A single axial location is shown, $z = 76 \pm 2 \text{ mm}$. Other heights were measured ranging from 5 mm above the end rings to the mid-height at 140 mm, but the mean profile does not differ significantly over this range.²⁵ Detailed measurements of velocity fluctuation levels made near the ring gap show the presences of residual boundary effects extending to $z = 40 \text{ mm}$, see Fig. 7. Scaling of the component speeds $\Omega_1, \Omega_3, \Omega_4, \Omega_2$ by a constant factor scales the radial profile of v_θ , by the same amount, as shown in Fig. 8.

V. DISCUSSION

We have constructed a unique rotating shear flow experiment capable of operation at high Reynolds number with active control of secondary circulation. The active control confines the effects of the boundary layers near the end caps. The apparatus is compatible with a liquid gallium alloy which is needed for studying MRI in a magnetized fluid. Engineering challenges which are imposed by high speed quiescent operation and gallium compatibility have been overcome. These challenges include supporting, or reducing where possible, the large dynamic pressures generated by high speeds and sealing the experiment against the loss of gallium.

ACKNOWLEDGMENTS

We appreciate J. Goodman, who suggested the topic of SHI and M. Nornberg, who proofed an early draft of this manuscript and suggested improvements. Technical and engineering work was provided by R. Cutler, P. Heitzenroeder, C. Jun, L. Morris, and S. Raftopolous of PPPL. Machining of the rotating assembly was performed by General Tool Co. of Cincinnati, OH, with additional machining performed by the Department of Physics Machine Shop, Princeton University and PPPL Tech Shop. This research was supported by the U.S. Department of Energy's Office of Science—Fusion Energy Sciences Program, the U.S. National Aeronautics and Space Administration's Astronomy and Physics Research and Analysis Program (Grant No. ATP03-0084-0106), and Astrophysics Theory Program (Grant No. APRA04-0000-0152), and also the U.S. National Science Foundation, Physics and Astronomical Sciences Divisions (Grant No. AST-0205903).

¹S. A. Balbus and J. F. Hawley, *Rev. Mod. Phys.* **70**, 1 (1998).

²H. Ji, J. Goodman, and A. Kageyama, *Mon. Not. R. Astron. Soc.* **325**, L1 (2001).

³D. Richard and J.-P. Zahn, *Astron. Astrophys.* **347**, 734 (1999).

⁴Y. Zeldovich, *Proc. R. Soc. London, Ser. A* **374**, 299 (1981).

⁵S. A. Balbus and J. F. Hawley, *Astrophys. J.* **376**, 214 (1991).

⁶S. Grossmann, *Rev. Mod. Phys.* **72**, 603 (2000).

⁷N. B. Morley, J. Burris, L. C. Cadwallader, and M. D. Nornberg, *Rev. Sci. Instrum.* **79**, 056107 (2008).

⁸M. Couette, *Compt. Rend.* **107**, 388 (1888).

⁹A. Mallock, *Proc. R. Soc. London* **45**, 126 (1888).

¹⁰L. Rayleigh, *Proc. R. Soc. London, Ser. A* **93**, 148 (1917).

¹¹G. Taylor, *Philos. Trans. R. Soc. London, Ser. A* **223**, 289 (1923).

¹²R. Tagg, *Nonlinear Sci. Today* **4**, 1 (1994).

¹³F. Wendt, *Ing.-Arch.* **4**, 577 (1933).

¹⁴G. Taylor, *Proc. R. Soc. London, Ser. A* **157**, 546 (1936).

¹⁵D. Richard, Ph.D. thesis, Université Paris 7, 2001.

¹⁶F. Schultz-Grunow, *Z. Angew. Math. Mech.* **39**, 101 (1959).

¹⁷H. Beckley, Ph.D. thesis, New Mexico Institute of Mining Technology, 2002.

¹⁸A. Kageyama, H. Ji, J. Goodman, F. Chen, and E. Shoshan, *J. Phys. Soc. Jpn.*, Part 1 **73**, 2424 (2004).

¹⁹H. Ji, M. J. Burin, E. Schartman, and J. Goodman, *Nature (London)* **444**, 343 (2006).

²⁰M. J. Burin, H. Ji, E. Schartman, R. Cutler, P. Heitzenroeder, W. Liu, L. Morris, and S. Raftopolous, *Exp. Fluids* **40**, 962 (2006).

²¹H. Greenspan, *The Theory of Rotating Fluids* (Cambridge University Press, London, 1968).

²²H. E. Albrecht, M. Borys, N. Damaschke, and C. Tropea, *Laser Doppler and Phase Doppler Measurement Techniques* (Springer, Berlin, 2003).

²³C. Rogers, *Phys. Fluids A* **3**, 928 (1991).

²⁴A. Townsend, *The Structure of Turbulent Shear Flow* (Cambridge University Press, London, 1980).

²⁵E. Schartman, Ph.D. thesis, Princeton University, 2008.